Journal of
Materials Chemistry A

Materials for energy and sustainability

rsc.li/materials-a

Volume 6
Number 12
28 March 2018
Pages 4883-5230

ISSN 2050-7488

**ROYAL SOCIETY
OF CHEMISTRY**

COMMUNICATION
Zhenhai Wen *et al.*
An electrochemically neutralized energy-assisted low-cost
acid-alkaline electrolyzer for energy-saving electrolysis
hydrogen generation

This is an Accepted Manuscript, which has been through the
Royal Society of Chemistry peer review process and has been
accepted for publication.

Accepted Manuscripts are published online shortly after acceptance,
before technical editing, formatting and proof reading. Using this free
service, authors can make their results available to the community, in
citable form, before we publish the edited article. We will replace this
Accepted Manuscript with the edited and formatted Advance Article as
soon as it is available.

You can find more information about Accepted Manuscripts in the
Information for Authors.

Please note that technical editing may introduce minor changes to the
text and/or graphics, which may alter content. The journal's standard
Terms & Conditions and the Ethical guidelines still apply. In no event
shall the Royal Society of Chemistry be held responsible for any errors
or omissions in this Accepted Manuscript or any consequences arising
from the use of any information it contains.

**ROYAL SOCIETY
OF CHEMISTRY**

rsc.li/materials-a

ARTICLE

Multiscale symbiotic carbonaceous silica nanofiber aerogels composed of ZrO₂ pinning structure with high-temperature thermal insulation and high strength

Pengzhan Yang, [ab†] Cui Liu, [ac†] Jiahao Zhu, [ad] Nian Li, [*ac] Shudong Zhang [*ac] and Zhenyang Wang [*ac]

Silica fiber aerogels often show considerably increased high-temperature thermal conductivity because of the weak infrared extinction ability, while showing limited mechanical strength. Improving infrared shielding and boosting structural strength are key challenges in achieving high-temperature insulation with SiO₂ nanofiber aerogels. Here, a multiphase sequence and multiscale structural engineering strategy is proposed to synthesize multiscale symbiotic carbonaceous SiO₂ nanofiber aerogels composed of ZrO₂ pinning structure to achieve high-temperature thermal insulating performance with high mechanical strength. ZrO₂ nanocrystalline pinning effect can effectively impede the formation of shear band and suppress the generation-migration of pores and micro-cracks of single amorphous SiO₂ nanofiber, enhancing thermal stability and mechanical strength. Besides, what is particularly impressive is that the design of the pinning structure can also stabilize high extinction symbiotic carbon species to achieve the presence of high content carbon, thereby suppressing the thermal radiation heat transfer to reduce high temperature thermal conductivity. Meanwhile, the layered assembly and coating construction at the mesoscale further enhance the antioxidant capacity of the aerogel. Finally, the 3D aerogel assembled in layers demonstrates outstanding mechanical properties (a compressive strength of 78.27 KPa at 60% strain and a tensile strength of 240.69 KPa, which is several times better than that of other ceramic fiber aerogels) and ultralow thermal conductivity over a wide temperature range (0.0935 W m⁻¹ K⁻¹ at 1000 °C, which is approximately one order of magnitude lower than that of conventional ceramic fiber aerogels). Our work provides a new option for heat insulation under extreme conditions.

Introduction

As the most classic inorganic thermal insulation material, silica aerogel has received extensive attention in the field of thermal insulation.[1-3] Compared with typical silica particle aerogel, silica aerogel composed of nanofibers shows excellent deformability, effectively addressing the contradiction between complex stress variations and thermal insulation performance in practical applications, thereby drawing significant attention from numerous researchers.[4-6] However, when the temperature is above 500 °C, thermal radiation becomes the predominant mode of heat transfer.[7] The low-density feature and high transmittance of silica nanofiber

aerogel will lead to strong thermal radiation heat transfer at high temperatures, and the thermal conductivity is often over 200 mW m⁻¹K⁻¹ around 1000 °C, posing a significant challenge to its application in the field of high-temperature insulation.[8,9] Therefore, addressing the decline in thermal insulation performance caused by thermal radiation is a critical research focus for SiO₂ nanofiber aerogels.

A potential strategy to reduce thermal radiation heat transfer is to incorporate high infrared opacifiers such as TiO₂ or carbon.[7,10] The incorporation of high infrared extinction agents can enhance the extinction capability of nanofibers, reduce the transmittance, significantly suppress thermal radiation, and exhibit excellent high-temperature thermal insulation performance.[8,11] The extinction ability increases with the increase of the extinction substance, thereby achieving better high-temperature thermal insulation performance.[12,13] However, because of the softening effect of TiO₂, the structural stability of aerogels will reduce.[14] Carbon species, with a specific extinction coefficient of 10^4 m² kg⁻¹, is one of the substances with the strongest extinction ability known to date, has been widely used in thermal insulation materials to suppress thermal radiation heat transfer.[15-17] Nevertheless, carbon species even wrapped by silica nanofibers, their oxidation resistance is insufficient because of the migration of SiO₂ at high temperatures and will be

a. Institute of Solid-State Physics, Hefei Institutes of Physical Science, Chinese Academy of Sciences, Hefei, Anhui, 230031, China. E-mail: sdzhang@iim.ac.cn; linian@issp.ac.cn;zywang@iim.ac.cn
b. University of Science and Technology of China, Hefei 230026, China.
c. The Key Laboratory of Photovoltaic and Energy Conservation Materials, Hefei Institutes of Physical Science, Chinese Academy of Sciences, Hefei, 230031, China.
d. Institutes of Physical Science and Information Technology, Anhui University, Hefei 230601, China.
† PZ Yang and C Liu contributed equally to this work.
Electronic supplementary information (ESI) available.

thermal etched in the air.[8] Therefore, improving the thermal and structural stability of SiO_2 nanofibers is a prerequisite for achieving the stability of carbon species within SiO_2.

The grain pinning effect is what crystals are embedded in amorphous matrices, and nanocrystalline domains function as rivets to restrict the migration of amorphous matrices at high temperatures, thereby enhancing the thermal and structural stability of the material.[7,8,18-21] The embedding of nanocrystals can impede the formation of amorphous structural shear bands and enhance mechanical strength.[7] More importantly, the pinning structure increases the energy barrier of oxygen activation to improve oxidation resistance, endowing excellent thermal stability.[8] The grain pinning effect provides new guidance for the manufacturing of nanofibers with excellent stability, which inspires us to explore and design highly stable ultra-light ceramic structures with similar structures. On the other hand, the reduced thermal protection effect of ceramic aerogel caused by high vapor pressure and oxygen permeation during long-term use is critical issues to be addressed[10]. The construction of high-temperature resistant protective layers can serve as an oxidation barrier, effectively slowing down the oxidation rate and enhancing structural stability[10,22]. AlSiB, a high-temperature resistant material, possesses a composition similar to that of ceramic fibers and exhibits a comparable coefficient of thermal expansion, showing good interfacial compatibility and is widely used in high-temperature thermal protection fields[6,10]. Therefore, the design of multi-scale structures can inspire us to design high-temperature thermal protection ceramic aerogels with excellent stability

Here, we propose a multiphase sequence and multiscale structural engineering strategy is proposed to synthesize multiscale symbiotic carbonaceous SiO_2 nanofiber aerogels composed of ZrO_2 pinning structure (SZC LFAs) to achieve a simultaneous improvement in high-temperature thermal insulating performance and mechanical strength. At the nanoscale, owing to the incorporation of ZrO_2 nanocrystalline phase, the pinning structure formed effectively pin the migration of amorphous matrix at high temperatures, reduce the generation of pores and micro-cracks, improve oxidation resistance, and achieve the retention of 8-16 at% high content carbon. The existence of high-content carbon species effectively suppresses thermal radiation and demonstrates excellent high-temperature insulation performance. And the pinning structure also suppresses crack propagation, enhances the fracture toughness and improves the mechanical strength. The design of nanoscale pinning structure endows the nanofiber building blocks with excellent thermal stability and mechanical strength. Finally, at the mesoscale, a three-dimensional elastic ceramic nanofiber aerogel with layered stacked structures was fabricated through sol impregnation combined with freeze-drying (SZC LFAs). Built an antioxidant layer on the nanofiber surface and form connection nodes between the nanofibers, further enhancing the antioxidant property and mechanical strength of the aerogel. Due to the multiscale structure design, ceramic aerogels exhibit ultralow thermal conductivity at high temperature (0.0935 W m^{-1} K^{-1} at 1000 ^oC) and high strength (a compressive strength of 78.27 KPa at 60% strain and a tensile strength of 240.69 KPa). Our research demonstrates significant potential for high-temperature insulation applications.

Experimental Section

Materials

Tetraethyl orthosilicate (TEOS) ($C_8H_{20}O_4Si$)，Oxalic acid ($C_2H_2O_4$), Polyethylene oxide (PVB), ethanol (EtOH) and Zirconium acetate ($C_8H_{12}O_8Zr$) were purchased from Aladdin Co., Ltd, China. Anhydrous aluminum chloride ($AlCl_3$) and Boric acid (H_3BO_3) were purchased from Sinopharm chemical reagent Co., Ltd.

Fabrication of SiO_2-ZrO_2/PVB Nanofiber Membranes

SiO_2-ZrO_2/PVB nanofibers film were fabricated via the electrospinning technique. First, TEOS, H_2O, ethanol, and $C_2H_2O_4$ were mixed in a molar ratio of 1:3.57:0.71:0.016, respectively. The mixture was stirred at room temperature for 8 h to obtain silica sol. Then zirconium acetate was added to the silica sol in different molar ratios (Zr: Si = 1:8,1:4 and 1:2) and stirred for 2 hours to obtain sol. Meantime, PVB was dissolved in ethanol solution and stirred for 8 h, the mass fraction was 15%. Next sol and polymer solution were mixed in a mass ratio of 1:1 and stirred for 2 h to obtain a stable precursor spinning solution. Finally, SiO_2-ZrO_2/PVB nanofibers film were fabricated via electrospinning. The spinning voltage is 20 KV, the rotating nozzle diameter is 0.6 mm, and the spinning temperature and humidity are 25 ^oC and 50%.

Fabrication of SZC NFs

SiO_2-ZrO_2/PVB nanofibers films with different doping amounts of Zr were calcined in argon gas at 1000 ^oC for 2 h to obtain SiO_2-ZrO_2-C nanofiber film (SZC NFs). Additionally, SiO_2-ZrO_2/PVB nanofibers film with Zr: Si=1:4 was calcined in argon gas at different temperatures for 2 hours to obtain SZC NFs at different temperatures.

Fabrication of SZC LFAs

First, 0.78 g $AlCl_3$, 3.04 g TEOS, and 0.36 g boric acid (H_3BO_3, 99.5%) were added sequentially to DI water and stirred constantly for 4 h to obtain clear AlSiB sol. Then, the SZC NFs were transferred into AlSiB sol and adsorption saturation, it was frozen at -80 $°C$ until complete solidification. The water was then removed by freeze-drying for 48 h. Finally, the dried aggregate was calcined at 800 ^oC for 2 h under Ar atmosphere to achieve surface ceramization.

Mechanical Testing

Mechanical tests were conducted using a universal testing machine equipped with 2000 N sensors (AGS-X, Japan Shimadzu). The loading and unloading rates were set to 2 mm min^{-1} for the compression test. The density of aerogels was 50 mg cm^{-3}. The compressive strains are 20%, 40%, 60% and 80%, respectively. The fatigue resistance of SZC LFAs were determined with a loading rate of 20 mm min^{-1} for 1000 cycles, the compressive strain was 50%. The tensile test was performed with a loading rate of 2 mm min^{-1}. The density of aerogels is 50 mg cm^{-3}.

The dynamic mechanical performances of SZC LFAs were evaluated by using a DMA (DMA850, USA Thermo Fisher) instrument within a manipulatable temperature range (-100 to 300 °C). The test frequency was 0.1Hz and the initial stress was 0.01N. The dynamic mechanical performances of the SZC LFAs with different frequency were tested under a prestressing force of 0.01 N and an oscillatory strain of 1%. The frequency range is 0.01-1 Hz.

Calculation of the extinction coefficient

The specific extinction coefficient is calculated based on the transmittance. The specific calculation process is as follows:

$$T = I/I_0 = e^{-\alpha l}$$

T represents the infrared transmittance, I and I_0 are the intensity of transmitted infrared light and the intensity of incident infrared light respectively. l is the thickness of the specimen, and α is the extinction coefficient, which is defined as the sum of the scattering coefficient and the absorption coefficient. The extinction coefficient can be expressed as α = e*·ρ, where e* is the specific extinction coefficient and ρ denotes the density. Based on this relationship, the value of e* can be determined:

$$e^* = -\frac{1}{\rho l} ln(I/I_0)$$

Thermal conductivity test

The three-dimensional size of the samples used in thermal conductivity measurements was 1 cm × 1 cm × 1 cm. The density of SZC LFAs is 50 mg cm^{-3}. Their thermal conductivities were measured by applying a Hot Disk instrument (TPS2500S, Switzerland KAITS) based on the ISO 22007 2:2015 standard.

Thermal insulation test

We heated the SZC LFAs with a height of 1.5 cm under an acetylene lamp for different times and recorded the temperature changes at different times using an infrared camera. Simultaneously, a 2 cm thick aerogel was wrapped around an acetylene spray gun, and then an infrared camera(Fluke TIs75， USA FLIR) was used to record the temperature changes at different times.

Characterization

The microstructure of SZC LFAs and SZC NFs were observed via scanning electron microscope (SEM, ZEISS of German). The elemental composition of nanofibers was examined with an energy dispersive spectrometer (EDS) equipped on the SEM system. The elements of the nanofiber were characterized by X-ray photoelectron spectroscopy (XPS, ESCALAB 250, USA Thermo Fisher). The crystal structure of the material was characterized by X-ray diffraction (XRD, X 'Pert, Holland PANalytical). Infrared transmittance was determined by the infrared spectrometer (FTIR, Bruker Nicolet iS50, USA Thermo Fisher).

Results and discussion

Design and Fabrication of SZC NFs

For silica nanofibers, the composition of the amorphous structure can trigger shear strain and show excellent deformability. However, the generation and propagation of microcracks under external forces render nanofibers prone to fracture, resulting in limited mechanical strength. Besides, the migration of amorphous phases at high temperatures generates many pores, compromising structural stability. As shown in Figure 1a and b, compared with amorphous structures (Model Ⅰ), the design of pinning structures (Model Ⅱ) can suppress the generation of microcracks, impede the formation of shear band and exhibit higher mechanical strength. On the other hand, the pinning structure can utilize the nanocrystalline domain as a rivet to effectively suppress the migration of the amorphous matrix at high temperatures, minimize the formation of pores, and demonstrate better structural stability.

Inspired by the pinning structure, symbiotic carbonaceous SiO_2 nanofiber composed of ZrO_2 pinning structure were fabricated by a simple electrospinning strategy to achieve high-temperature insulation and high mechanical strength (SZC NFs). Firstly, silica sols with different zirconium (Zr) contents were mixed with polyvinyl alcohol butyraldehyde solution to prepare the spinnable precursor solution. By optimizing conditions such as spinning voltage (Table S1), precursor concentration (Table S2) and spinning liquid feed rate (Table S3), combined with morphology analysis (Figure S1), the optimal spinning conditions are obtained, which were 20kV voltage, a feed rate of 0.2mL/min, and a precursor concentration of 15wt%. Under this condition, nanofibers with an average diameter of approximately 887 nm were successfully fabricated using electrospinning and carbonization (Figure 1c-d). With the increase of zirconium content, the SZC NFs diameter gradually increases (Figure S2), and the surface becomes smoother (Figure S3). This phenomenon may be attributed to the reduction in surface energy and the elevated volatility of the precursor sol.[23] TEM indicates that ZrO_2 nanocrystals are uniformly embedded in amorphous structure (Figure 1e-f), The lattice spacing is approximately 0.292 nm, which corresponds to the (111) crystal plane of ZrO_2 (Figure S4). The FFT pattern further confirms the successful intercalation of the ZrO_2 crystal (Figure 1f and S4). XRD also indicates that tetragonal zirconia nanocrystals were successfully introduced into the nanofibers (Figure 1g), and the intensity of the X-ray diffraction peaks increases with higher annealing temperature, indicating increasing crystallization (Figure S5). Then, carbon components can be incorporated into the interior of nanofibers through the carbonization process. The two prominent peaks at 1350 cm^{-1} (D-band) and 1590 cm^{-1}(G-band) in the Raman spectrum indicates the presence of carbon (Figure 1h). XPS confirmed the incorporation of Zr and C into the silica nanofibers (Figure 1i and S6), and the high-resolution XPS spectra of Zr and Si indicate that an interfacial interaction has formed between the embedding of ZrO_2 and the amorphous SiO_2 matrix (Figure S7)[24]. Additionally, EDS also indicated Zr and C elements are uniformly incorporated into the silica nanofibers (Figure 1j).
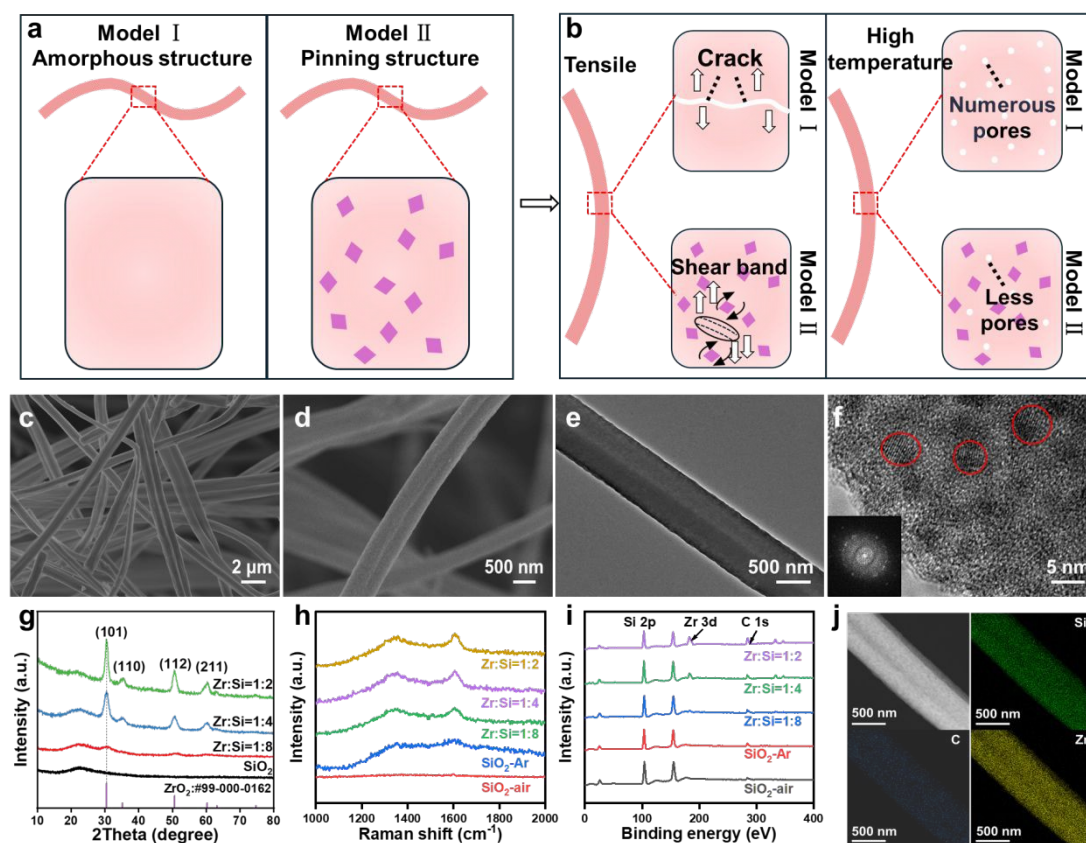
ARTICLE

Fig. 1 Preparation process for SZC NFs. (a) Schematic diagrams of different structural models. (b) The structural evolution mechanisms of different structural models under tensile and high temperature conditions. (c-d) SEM images of SZC NFs with Zr:Si=1:4. (e-f) TEM images of nanofibers containing ZrO$_2$ nanocrystalline phase with Zr:Si=1:4(The illustration shows the FFT mode of TEM). (g) XRD patterns with different Zr molar ratio. (h) Raman patterns with different Zr molar ratio. (i) XPS of different Zr molar ratios. (j) Mapping of SZC NFs.

The influence of mechanical performance

Different ZrO$_2$ nanocrystals contents significantly influence the mechanical properties. The maximum tensile strength of SiO$_2$ nanofiber membrane is 15.3 KPa. With the increase of Zr content, the tensile strength of the nanofiber membrane gradually increases. When Zr:Si=1:2, the tensile strength reaches 151.1 KPa (Figure 2a). The increase in tensile strength is mainly attributed to the introduction of ZrO$_2$ nanocrystalline phase. The intercalation of the nanocrystal phase introduces more solid chemical bond interactions and impede the formation of shear band, thereby demonstrating higher tensile strength.[25] The XRD shows that with the introduction of Zr, the crystallinity increases, indicating that a large number of solid chemical bonds are introduced inside the fibers, thereby enhancing the tensile strength (Figure S8). The XPS results also indicate that as the Zr content increases, more ZrO$_2$ crystals are introduced into the fiber interior, further enhancing the tensile strength (Figure 1i). On the other hand, with the increase of the Zr/Si ratio, the tensile toughness initially increases and subsequently

decreases. When Zr:Si=1:4, the tensile toughness reaches 1072.1 J m^{-3} (Figure 2b). And the annealing temperature also exerts a substantial influence on the mechanical properties. As the annealing temperature increases, the tensile strength gradually increases, and the strength is 170.67 KPa at 1200 °C (Figure 2c). The enhancement in strength can primarily be attributed to the increased crystallinity of ZrO$_2$ nanocrystals within the nanofibers as the annealing temperature rises, the grain size gradually enlarges (Figure S9), intermolecular stacking tightness between crystalline molecules improves, and the slip of amorphous molecular chains diminishes, all contributing to the enhanced strength of the nanofibers.[26] The tensile toughness reached 1557.09 J m^{-3} at 1000 °C and subsequently decreased.

The mechanism of increased toughness can be attributed to the deflection effect of microcracks (Figure 2e). Under external loading, fracture microcracks will occur inside silica fibers. As the stress increases, the microcracks will continuously expand and eventually break. When nanocrystals are introduced, numerous nanocrystalline

ARTICLE

domains similar to nails will form inside the fibers, which can compel microcracks to either deflect around the nanocrystals or terminate at the nanocrystal/matrix interface, increase the energy required for fracture, and thus enhance the toughness of the fibers.[27,28] Excessive nanocrystals can lead to crystal aggregation, causing grain boundary cracking and resulting in a decrease in toughness.[29] On the other hand, as the temperature increases, ZrO_2 nanocrystals continuously grow and expand, during the tensile process, significant stress concentration occurs at the enlarged grains, resulting in increased brittleness and decreased toughness of the nanofibers.[25]
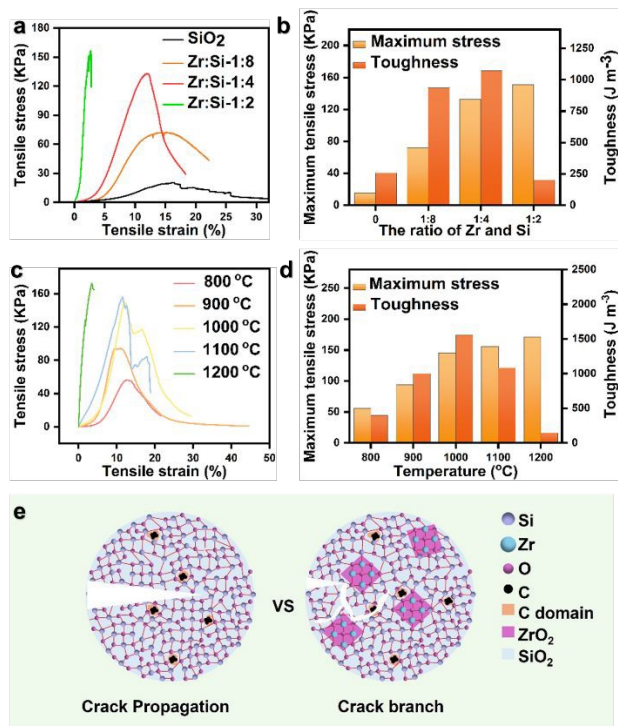

Fig. 2 The influence of mechanical performance. (a) Tensile stress–strain curve of different Zr contents. (b) Maximum tensile strength and toughness of different Zr contents. (c) Tensile stress–strain curve of different annealing temperatures. (d) Maximum tensile strength and toughness of different annealing temperatures. (e) The mechanism of the ZrO_2 nanocrystalline phase enhancing the amorphous phase of SiO_2.

The influence of thermal insulation performance

The presence of carbon species can effectively suppress thermal radiation and reduce the thermal conductivity at high temperatures. Different ZrO_2 nanocrystals influence the carbon content inside SZC NFs, which in turn affects the thermal insulation performance. At the same carbonization temperature (1000 °C), with the content of ZrO_2 increases, the colour of SZC NFs membrane gradually darkens (Figure S10), and the intensity of the C peak in XPS also progressively increases (Figure 1d and S11), indicating that the carbon content inside the fiber increases accordingly. Thermogravimetric analysis further demonstrated that an increase in Zr content corresponded with an increase in the carbon content within the fibers (Figure S12). This might be due to the embedding of ZrO_2 nanocrystals forming a pinned structure. Zirconia grains can restrict the migration of amorphous matrixes at high temperatures, reduce the generation of

pores and micro-cracks, improve the antioxidant capacity and enhance the thermal stability of carbon components at high temperatures,[7,8] achieve the retention of high-load carbon. Compared with carbon-free silica fibers, the incorporation of carbon significantly reduces the transmittance of ceramic fibers at wavelengths of 3-15 μm. And the transmittance gradually decreases with the increase of carbon content, when Zr:Si=1: 2, the transmittance drops to approximately 65% (Figure 3a). Furthermore, as the carbon content increases, the specific extinction coefficient of the SZC NFs gradually increases, when Zr:Si= 1:2, the specific extinction coefficient increases by an order of magnitude (Figure 3b). The significant increase in the specific extinction coefficient notably diminished the thermal conductivity of SZC NFs at high temperatures. In comparison to carbon-free silica nanofiber aerogels (0.129 W m^{-1} K^{-1}), the thermal conductivity of SZC NFs aerogel corresponding to the Zr:Si ratio of 1:2 decreased by 32.7%, reaching a value of 0.0867 W m^{-1} K^{-1}. The introduction of carbon components can increase the specific extinction coefficient and significantly reduce the high-temperature thermal conductivity (Figure 3c). The carbon content gradually decreases with the increase of annealing temperature (Figure 3d), leading to a gradual increase in transmittance (Figure S13). And the corresponding specific extinction coefficient also decreases (Figure 3e). And at the annealing temperature of 1200 °C, the thermal conductivity corresponding to 1000 °C is 0.114 W m^{-1} K^{-1}, which is significantly lower than that of carbon-free SiO_2 nanofiber aerogel (0.129 W m^{-1} K^{-1}), showing excellent high-temperature thermal insulation performance (Figure 3f). By optimizing the experimental conditions, when Zr:Si=1:4 and the annealing temperature is 1000 °C, the high tensile performance and low high-temperature thermal conductivity can be balanced. Subsequent experiments will be conducted under these conditions

The Mechanical properties of SZC LFAs

To ensure the long-term use of thermal insulation materials under high-temperature conditions, it is still necessary to further enhance their oxidation resistance. Subsequently, the prepared SZC NFs were assembled in layers in the AlSiB sol to obtain a 3D elastic ceramic aerogel with a cross-linked network (SZC LFAs) (Figure S14). SZC LFAs shows a layered stacked structure (Figure S15a). Through gel impregnation and ice crystal growth, AlSiB gel not only coats the surface of the fibers but also forms a 2D surface bridging network between the nanofibers (Figure S15b-c). TEM indicates that AlSiB is coated on the surface of the fibers. With the increase of AlSiB concentration, the thickness of the nano-coating on the fiber surface gradually increases, significantly affecting the antioxidant capacity and mechanical properties (Figure S16). A thicker nano-coating results in a less pronounced color change when the material is exposed to heat from an acetylene flame (Figure S17). Thermogravimetric analysis further confirms that increased coating thickness correlates with reduced weight loss, suggesting that thicker coatings substantially enhance antioxidant performance (Figure S18). Additionally, the compression test curve demonstrates that while greater coating thickness improves compressive strength, it simultaneously reduces elasticity (Figure S19). Therefore, by appropriately adjusting the AlSiB concentration, it is possible to achieve a balanced enhancement of both antioxidant capacity and

mechanical properties. EDS and XPS also confirm that the presence of Al, Si and B elements (Figure S20 and S21). SZC LFAs with cross-linked networks exhibits exceptional mechanical properties.
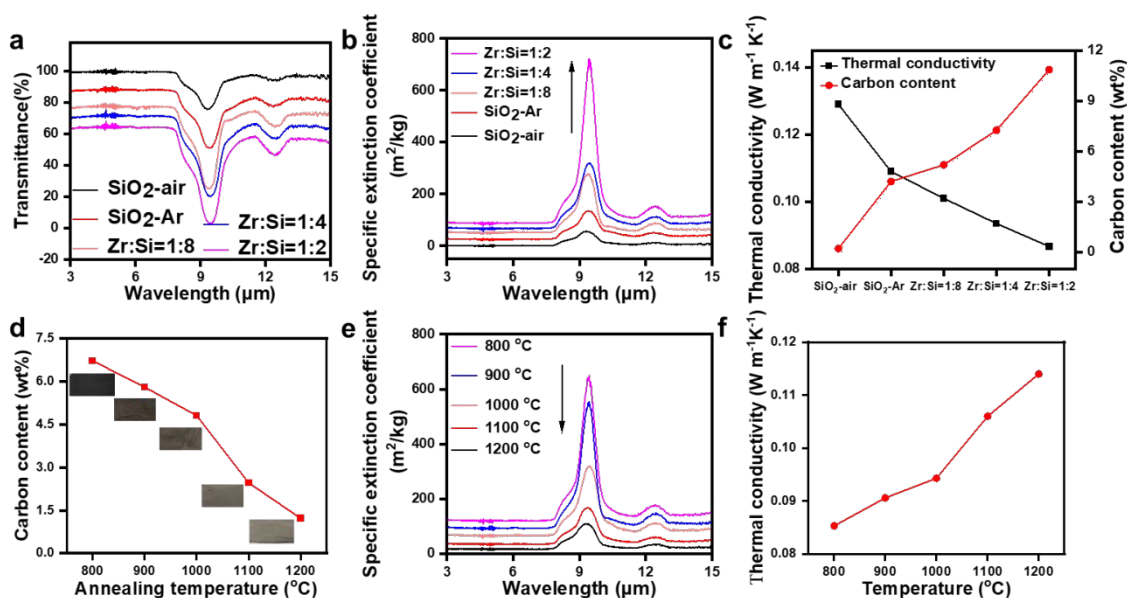
Fig. 3 The influence of thermal insulation performance. (a) Infrared transmittance of different Zr contents. (b) Specific extinction of different Zr contents. (c) The change of carbon content under different Zr contents and the corresponding thermal conductivity at 1000 °C. (d) The change of carbon content under different annealing temperatures (Inset picture: Color changes of fiber membranes under different annealing temperatures). (e) Specific extinction of different annealing temperatures. (f) The thermal conductivity at 1000 °C under different annealing temperatures.

The quasi-static compressive stress-strain curve of SZC LFAs indicates that it can recover to the initial state after 60% compressive strain, and the plastic deformation is only 12.68%, indicating excellent resilience performance (Figure 4a). Notably, at a compressive strain of 60%, the maximum compressive strength reaches 78.27 KPa, indicating that the aerogel can support a load exceeding 8000 times its own weight, which is at the leading level compared with other ceramic nanofiber aerogels (Figure 4b). And after being subjected to a compressive force exceeding 10,000 times its own weight for 12 h, the height of SZC LFAs remained basically unchanged, indicating its excellent compressive resistance (Figure S22). The excellent compression performance is attributed to the formation of the welded nodes. Specifically, the AlSiB high-temperature binder creates a connecting network among the nanofibers, effectively inhibiting the sliding of the nanofibers and enhances rigidity, while the nanofibers remain flexible, thereby obtaining aerogels with high elasticity and high strength (Figure S23).

The compression cycle test demonstrates that SZC LFAs retains excellent compression resilience performance after 500 cycles at 50% strain (Figure 4c), and the maximum compression stress at the 500th time is 75% of the initial. Additionally, the energy loss coefficient gradually decreased from the initial value of 0.49 to the stable value of 0.31 (Figure 4d), indicating that that SZC LFAs exhibits better mechanical robustness to a certain extent under external forces.
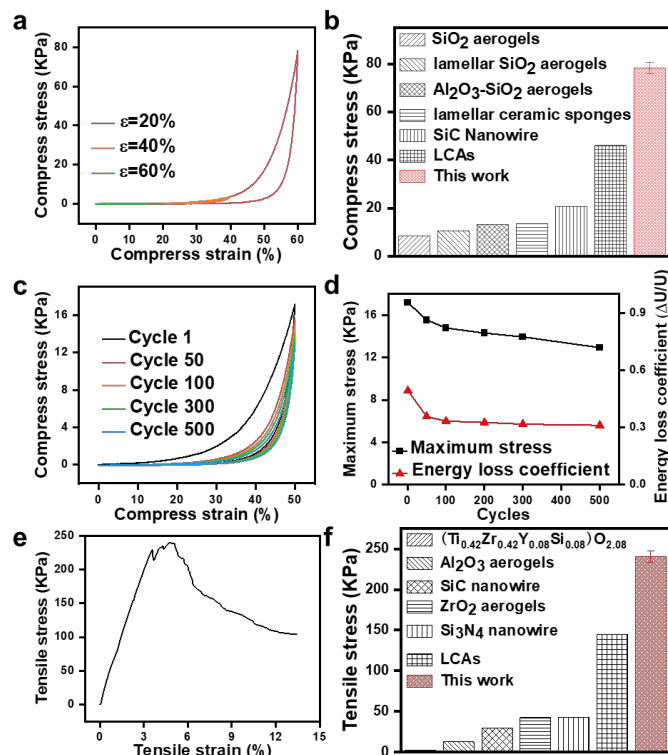

Fig. 4 Mechanical properties of SZC LFAs. (a) Compression of SZC LFAs with various strains (ε) up to 60%. (b) Comparison of the compressive strength of SZC LFAs and other reported ceramic fiber aerogels.[4,5,10,30,31] (c) A 500-cycle fatigue test with a compressive strain of 50%. (d) Maximum stress and energy loss coefficient versus compressive cycles. (e) Tensile stress–strain curve of SZC LFAs. (f)

Comparison of the tensile strength of SZC LFAs and other reported ceramic fiber aerogels.[7,9,10,19,31,32]

Besides the compressive performance, SZC LFAs also demonstrates excellent tensile performance. The tensile stress-strain curve reveals that as the tensile strain increases, the stress initially exhibits a linear rise. When the tensile strain reaches 4.8%, the aerogel exhibits the maximum tensile strength of 240.69 KPa (Figure 4e), which is superior to other common ceramic nanofiber aerogels (Figure 4f). Meanwhile, SZC LFAs can stretch weights over 2000 times its own weight, further demonstrating the excellent tensile strength (Figure S24).

The stability of SZC LFAs

To further evaluate the thermal stability of SZC LFAs under different conditions, dynamic mechanical analysis (DMA) was employed to evaluate the dynamic compressive behavior of aerogel at different temperatures and frequencies. As shown in Figure 5a-c, at different testing temperatures, the energy storage modulus is approximately one order of magnitude greater than the loss modulus. When the oscillation strain is 1% at a frequency ranging from 0.01 to 1Hz, the damping ratio remains constant, highlighting the predominance of elasticity and demonstrating the superior mechanical robustness of the aerogel. Meanwhile, due to the viscoelastic properties of the layered aerogel, the energy storage modulus and loss modulus of the

aerogel remain basically constant within the range of -100 to 300 °C, and the damping ratio is approximately 0.1, indicating that SZC LFAs exhibits excellent temperature invariability (Figure 5d). In addition, in-situ compression tests were conducted under extreme conditions of acetylene lamps and liquid nitrogen (Figure 5e). SZC LFAs can withstand multiple compressions and fully recover original shape under both low or high temperature conditions, demonstrating excellent low/high temperature resistance and thermal stability.

On the other hand, the presence of the surface coating enables SZC LFAs to exhibit superior antioxidant properties. When continuously heated in the air under an acetylene lamp for 10 min, the surface color of SZC LFAs basically remained unchanged, while the surface color of the layered ceramic-carbon fiber aerogel without the AlSiB coating (SZC NFs) turned white (Figure S25). This phenomenon can be attributed to the gradual etching of carbon at high temperatures. Additionally, the thermogravimetric curve demonstrates that due to the protection of the surface coating, SZC LFAs shows negligible weight loss when heated from room temperature to 800 °C in air, while SZC NFs exhibits approximately 8% weight loss (Figure 5f). The results further prove the protective effect of the surface coating on carbon components. Figure 5g reveals the thermal protection mechanism of the antioxidant coating. The anti-oxidation coating acts as a barrier, significantly delaying the spread of flames, the entry of oxygen and the outflow of volatile compounds, thereby reducing the rate of oxidation reactions.
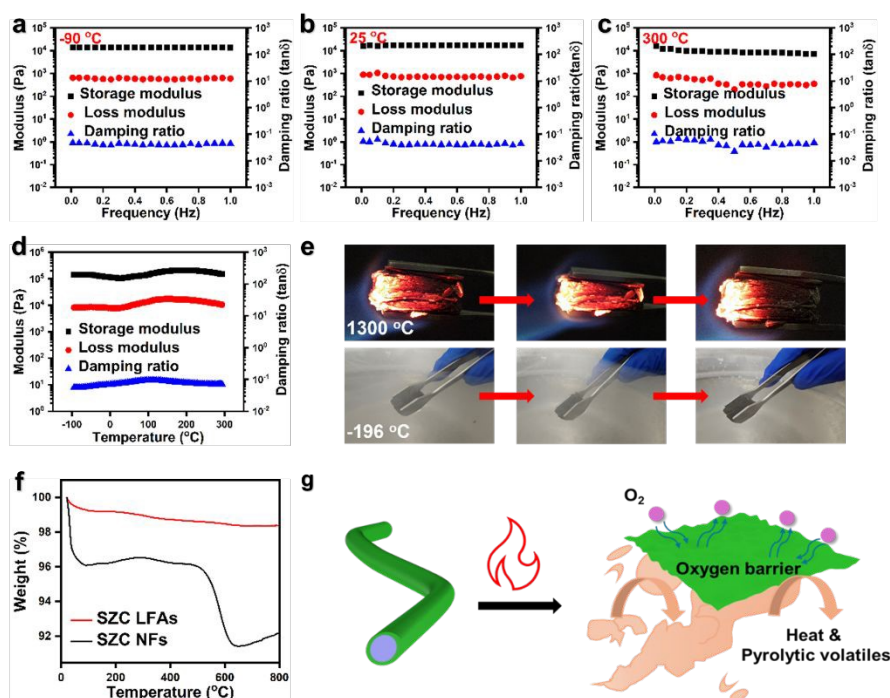

Fig. 5 The stability of SZC LFAs. (a-c) Storage modulus, loss modulus, and damping ratio of the SZC LFAs as a function of angular frequency from 0.01 to 1 Hz at temperatures of -90 °C, 25 °C and 250 °C. (d) Viscoelastic stability of the SZC LFAs at T = -100 to 250 °C (frequency of 0.1 HZ, oscillatory strain of 1%). (e) Snapshots of compressive views of SZC LFAs under high-temperature butane flame (∼1300 °C) or liquid nitrogen (∼-196 °C). (f) TG curves of SZC LFAs and SZC NFs under air. (g) Schematic diagram of thermal protection of SZC LFAs.

Thermal Insulation Performance

One of the most critical requirements for thermal insulation materials is low thermal conductivity over a wide temperature range. Generally, thermal conductivity is primarily composed of solid-phase thermal conductivity, gas-phase thermal conductivity, and radiative

thermal conductivity.[33-36] For SZC LFAs (Figure 6a), the complex transport pathways formed by ceramic fibers and nanosheets can effectively dissipate heat and reduce solid-phase heat conduction. And the design of the heterostructure and the formation of the multiphase interface result in a large amount of phonon scattering

and increase the interface thermal resistance. Consequently, the thermal conductivity at 25 °C is measured to be 0.0257 W m^{-1}K^{-1} (Figure 6b). As the temperature increases, thermal radiation becomes the predominant mode of heat transfer. Based on the calculation formula for radiant thermal conductivity (Kr):[8,10]

$$K_r = \frac{16}{3}\frac{n^2\sigma T^3}{\rho e}$$

n is the refractive index, σ is the Stefan-Boltzmann constant, ρ is the density, and e is the specific extinction coefficient. The relationship between radiation intensity and wavelength can be described as follows:[37]

$$E_\lambda = \frac{C_1\lambda^{-5}}{\exp\left[\frac{C_2}{\lambda T}\right]-1}$$

C_1 is the first radiation constant of 3.7415×10^8 W μm^4 m^{-2}, C_2 is the second radiation constant of 1.43879×10^4 μm K. According to Planck's law, the radiation intensity increases as temperature rises, and the wavelength corresponding to the maximum radiation intensity shifts toward shorter wavelengths. For infrared thermal radiation, it is mainly concentrated in the near-infrared and mid-infrared regions.[7] Therefore, reducing the specific extinction coefficient within this wavelength range is the main way to reduce thermal radiation. As mentioned above (Figure 3b and 3e), the incorporation of C can substantially decrease the specific extinction coefficient and enhance the extinction capability of SZC LFAs. SZC LFAs with high extinction capacity exhibits ultra-low thermal conductivity of 0.0935 W m^{-1}K^{-1} at 1000 °C (Figure 6b).
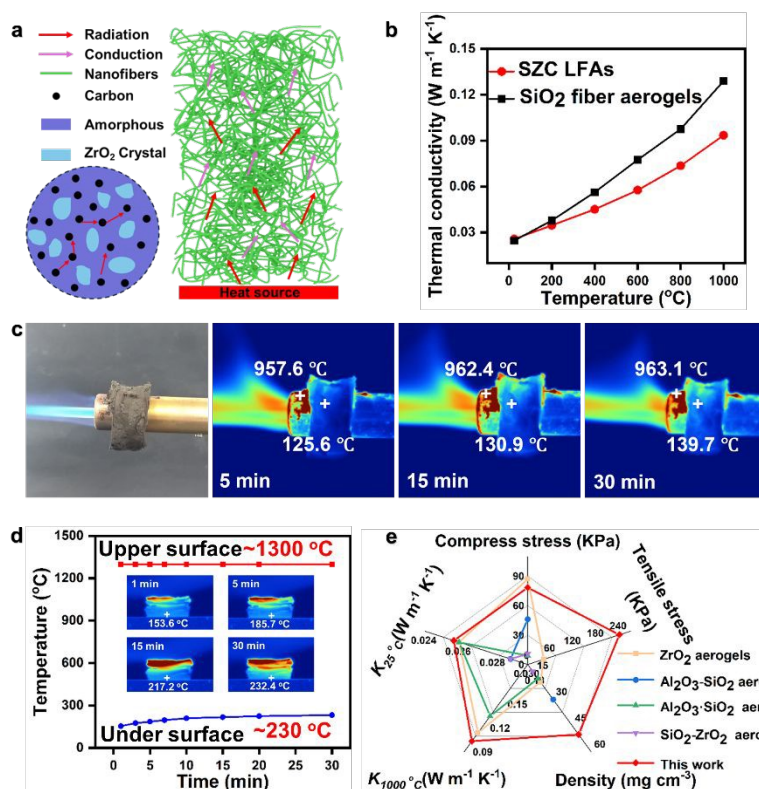

Fig. 6 Thermal Insulation Performance. (a) Schematics illustrate heat transfer in SZC LFAs including conduction, convection and radiation. (b) Thermal conductivity of SZC LFAs at different temperatures. (c) Optical and infrared images of SZC LFAs wrapped on the surface of the acetylene spray gun (flame temperature: ~1300°C) for 30 min. (d) SZC LFAs Temperature curves of the upper and lower surfaces under an acetylene spray gun (illustration of SZC LFAs optical and infrared images exposed to butane burner flame (flame temperature: ~1300°C) for 30 min.) (e) The comprehensive performance comparison of the aerogels with other reported ceramic aerogels.

We applied a 2 cm thick aerogel coating on acetylene blowtorch tubes for applications requiring isolated heat transfer. As shown in Figure 6c, when a flame reaching up to 1300 °C is emitted from the lamp tube, the temperature on the back of the aerogel progressively increases over time. After heating for 30 min, the temperature on the back of the aerogel was only 139.7 °C, indicating the excellent thermal insulation performance of the aerogel.

To further evaluate the thermal insulation performance of the aerogel, SZC LFAs with a height of 1.5 cm were placed under an acetylene lamp and subjected to heating for 30 min (Figure 6d). The infrared image revealed that after 1 min of heating, the temperature

of the lower surface of the aerogel was 153.6 °C. When heated for 30 min, the temperature of the lower surface of the aerogel rose to 232.4 °C, which was much lower than the 1300 °C of the upper surface. For SiO₂ nanofiber aerogel (Figure S26), the temperature of the lower surface reached 289.5°C after 30 min of heating, markedly higher than that of SZC LFAs. The result indicates that SZC LFAs with a multi-scale structure design demonstrated excellent thermal insulation performance. Finally, a comprehensive comparison was conducted between the thermal and mechanical properties of SZC LFAs and those of other advanced ceramic fiber aerogels (Figure 6e). The results indicated that SZC LFAs exhibited excellent mechanical

and thermal insulation properties, demonstrating great application potential in the field of thermal insulation.[7,39-41]

Conclusions

Our work proposed a multi-scale structural design strategy and successfully prepared elastic carbon-rich dual-phase nanofiber aerogel, demonstrating excellent mechanical and thermal properties. The exceptional performance can be primarily attributed to: i) the pinning structure formed by the incorporation of ZrO_2 nanocrystalline phase effectively pin the migration of amorphous matrix at high temperatures, reduce the generation of pores and micro-cracks, increases the energy required for fracture, thereby enabling the nanofibers to exhibit higher strength and tensile toughness. ii) the pinning structure stabilizes high extinction symbiotic carbon species to achieve the presence of high content carbon, thereby suppressing the thermal radiation heat transfer to reduce high temperature thermal conductivity. When the annealing temperature is 1000 °C with a Zr:Si ratio of 1:4, a balance between high mechanical properties and low high-temperature thermal conductivity can be successfully achieved. iii) At the microscale, the construction of AlSiB surface coating/network covering nanolayers not only protects the thermal etching of carbon and enhances the thermal stability of the nanofibers, but also forms cross-linked nodes between the nanofibers, further strengthening the mechanical strength of the aerogel. Owing to the design of the multi-scale structure, SZC LFAs exhibits excellent mechanical strength (a compressive strength of 78.27 KPa at 60% strain and a tensile strength of 240.69 KPa) as well as remarkable thermal insulation properties (thermal conductivity of 0.0935 W m^{-1} K^{-1} at 1000 °C). Our work provides promising materials for thermal protection under extreme conditions, but there is still a need to further enhance the long-term antioxidant capacity in high-temperature and oxygen-rich environments to expand its long-term application capabilities. In the future, scaling up the preparation of high-temperature thermal insulation aerogels and improving their thermal stability during prolonged use for widespread application in aerospace, national defense, fire protection, and other relevant fields will be a key challenge to address.

Author contributions

Pengzhan Yang and Cui Liu: designed the experiments, investigated and collected data, and drafted the manuscript. Jiahao Zhu and Nian Li: investigated data, writing original draft. Shudong Zhang and Zhenyang Wang: designed idea, discussed and analyzed the data, revised and edited the manuscript.

Conflicts of interest

There are no conflicts to declare.

Data availability

All data generated in this study are provided in the Source Data file. Source data are provided with this paper.

Acknowledgements

Notes and references

1   S. S. KISTLER, *Nature*,1931, **127**, 741.
2   S. Zhao, G. Siqueira, S. Drdova, D. Norris, C. Ubert, A. Bonnin, S. Galmarini, M. Ganobjak, Z. Pan, S. Brunner, G. Nyström, J. Wang, M. M. Koebel and W. J. Malfait, *Nature*,2020, **584**, 387-392
3   R. Wordsworth, L. Kerber and C. Cockell, *Nat Astron.*, 2019,**3**, 898-903.
4   Y. Si, X. Wang, L. Dou, J. Yu, and B. Ding, *Sci. Adv.*,2018,**4**, eaas8925.
5   L. Dou, X. Zhang, H. Shan, X. Cheng, Y. Si, J. Yu and B. Ding, *Adv. Funct.Mater.*,2020,**30**,2005928.
6   X. Zhang, C. Liu, X. Zhang, Y. Si, J. Yu and B. Ding, *J. Mater. Chem. A*, 2021,**9**, 27415-27423
7   J. Guo, S. Fu, Y. Deng, X. Xu, S. Laima, D. Liu, P. Zhang, J. Zhou, H. Zhao, H. Yu, S. Dang, J. Zhang, Y. Zhao, H. Li and X. Duan, *Nature*,2022,**606**,909-916.
8   S. Fu, D. Liu, Y. Deng, J. Guo, H. Zhao, J. Zhou, P. Zhang, H. Yu, S. Dang, J. Zhang, H. Li and X. Xu, *Nano Res.*,2023,**16**,5047-5055.
9   X. Xu, S. Fu, J. Guo, H. Li, Y. Huang and X. Duan, *Mater. Today*, 2021, **42**, 162–177.
10 X. Chang, Y. Yang, X. Cheng, X. Yin, J. Yu, Y. Liu and Bin Ding, *Adv.Mater.*,2024,**36**, 2406055.
11 A. A. Balandin, *Nat. Mater.* 2011, **10**, 569–581.
12 Q. Wu, M. Yang, Z. Chen, L. Lu, Z. Ma, Y. Ding, L. Yin, T. Liu, M. Li, L. Yang, B. Hou, H. Zhu and S. Cui, *J Mater. Sci. Technol.*,2025,**204**, 71-80.
13 S. Chen, K. Shen, Z. Chen, Q. Wu, L. Yan, Q. Zheng, Z. Zhang, L. Yin, B. Hou and H. Zhu, *Ceram. Int.*,2024,**50**, 17836-17847.
14 Y. Liu, M. Zhang, Y. Wang, Y. Zhang, J. Song, Y. Si, J. Yan, C. Ma, J. Yu and Bin Ding, *Angew. Chem. Int. Ed.*,2020,**132**,23452-23460.
15 G. Wei, Y. Liu, X. Zhang, F. Yu and X. Du, *Int. J. Heat Mass Transf.*, 2011, **54**, 2355–2366.
16 T. Choi, S. H. Kim, S. P. Jang, L. Lin and M A Kedzierski, *Energy*, 2020, **210**, 118523.
17 H. Liu, X. Xia, X. Xie, Q. Ai and D. Li, *Int. J. Therm. Sci.*, 2017, **121**, 192-203.
18 L. Li, C. Jia, Y. Liu, B. Fang, W. Zhu, X. Li, L. Schaefer, Z. Li, F. Zhang, X. Feng, N. Hussain, X. Xi, D. Wang, Y. Lin, X. Wei and H. Wu, *Mater. Today*,2022,**54**, 72-82.
19 S. Fu, D. Liu, Y. Deng, M. Li, H. Zhao, J. Guo, J. Zhou, P. Zhang, C. Wang, H. Yu, S. Dang, J. Zhang, M. Hao, H. Li and X. Xu, *J. Mater. Chem. A*, 2023, **11**, 742–752.
20 L. Xu, W. Zhou, L. Huang, J. Yu, Y. Si and B. Ding, *J. Mater. Chem. A*, 2024,**12**, 8311-8318.
21 X. Meng, C. Liu, J. Zhang, W.Guo, N. Li, Y. Chen, H. Xu, M. Xi, S. Zhang and Z. Wang, *J. Mater. Chem. A*,2024,**12**, 16079-16086.
22 Q. Yuan, L. Yan, J. Tian, W. Ding, Z. Heng, M. Liang, Y. Chen and H. Zou, *ACS nano*, 2024, 18, 3520-3530.

Journal of Materials Chemistry A Accepted Manuscript

23 L. Li, B. Fang, D. Ren, L. Fu, Y. Zhou, C. Yang, F. Zhang, X. Feng, L. Wang, X. He, P. Qi, Y. Liu, C. Jia, S. Zhao, F. Xu, X. Wei and H. Wu, *ACS Nano*, 2022, **16**, 10729-10741.

24 Wu C, Jiang J, Dong C, Zhao L, Liu J, Liu C, Deng H, Hui K N, Pang H, Yan Y, Liu M, *Adv. Funct. Mater.*, 2025, 2505742.

25 F. Wu, Y. Liu, Y. Si, J. Yu and B. Ding, *Nano Today*, 2022, **44**, 101455.

26 X. Zhang, Y. Liu, Y. Si, J. Yu and B. Ding, *Compos. Commun.*, 2022, **33**, 101219.

27 C. He, X. Shao, S. Yuan, L. Peng, Y. Wu, Q. Wang and Q. Chen, *Mater. Sci. Eng. A*, 2019, **744**, 716-723.

28 X. Xu, Y. Wang, A. Guo, H. Geng, S. Ren, X. Tao and J. Liu, *Int. J. Plast.*, 2016, **79**, 314-327

29 S. Qiang, F. Wu, H. Liu, S. Zeng, S. Liu, J. Dai, X. Zhang, J. Yu, Y. Liu and B. Ding, *Nat. Commun.*, 2025, **16**, 3265.

30 C. Jia, L. Li, Y. Liu, B. Fang, H. Ding, J. Song, Y. Liu, K. Xiang, S. Lin, Z. Li, W. Si, B. Li, X. Sheng, D. Wang, X. Wei and H. Wu, *Nat. Commun.*, 2020, **11**, 3732.

31 L. Su, H. Wang, M. Niu, X. Fan, M. Ma, Z. Shi and S. Guo, *ACS Nano*, 2018, **12**, 3103-3111.

32 M. Li, L. Su, H. Wang, P. Wan, P. Guo, Z. Cai, H. Gao, Z. Zhang and D. Lu, *Small*, 2021, **17**, 2100556.

33 X. Zhang, X. Cheng, Y. Si, J. Yu and Bin Ding, *ACS Nano*, 2022, 16, 5487–5495.

34 X. Zhang, F. Wang, L. Dou, X. Cheng, Y. Si, J. Yu and Bin Ding, *ACS Nano*, 2020, **14**, 15616–15625.

35 X. Zhang, J. Yu, C. Zhao and Y. Si, *ACS Nano*, 2023, **17**, 21813–21821.

36 X. Zhang, W. Huang, J. Yu, C. Zhao and Y. Si, *Adv. Funct. Mater.*, 2024, **35**, 2416857.

37 Z., Joanne, *Cham: Springer International Publishing*, 2023, 110-114.

38 F Huang, X Shen, G Li, G Wang and Z Zhao, *Opt. Eng.*, 2012, **51**, 086402.

39 L. Li, Y. Zhou, Y. Gao, X. Feng, F. Zhang, W. Li, B. Zhu, Z. Tian, P. Fan, M. Zhong, H. Niu, S. Zhao, X. Wei, J. Zhu and H. Wu, *Nat. Commun.*, 2023, **14**, 5410.

40 R. Zhang, C. Ye and B. Wang, *J Porous Mat.*, 2018, 25, 171–178.

41 Y. Cheng, B. Ma, P. Hu, J. Zhang, D. Hu and J. Wang, *Adv. Funct. Mater.*, 2023, **33**, 2309148.

Data availability

The data supporting this article have been included as part of the Supplementary Information.